of sequence introgression between *N. vitripennis* and *N. longicornis* (*18*). These results indicate that regulatory evolution of *upd-like* probably occurred in two separate *Nasonia* lineages, either by parallel reductions in *N. vitripennis* and *N. longicornis* or by reduction in an ancestral *Nasonia* lineage followed by expansion in the *N. giraulti* lineage. This observation plus the role of three subregions that we have identified between *N. vitripennis* and *N. giraulti* suggests that *unpaired-like* is a hotspot for wing size evolution in *Nasonia*.

Discussion. This study determined the genetic basis of *wdw*, a major component of the male-specific wing size difference between *N. vitripennis* and *N. giraulti*. Our data indicate that *upd-like* causes the spatial changes in cell proliferation and growth within the wing and that *upd-like* is a hotspot for size and shape evolution in *Nasonia*. *Unpaired* (*upd*) in *D. melanogaster* is a ligand for the JAK/STAT pathway (*21*). This pathway's role in cell proliferation makes it a plausible target of morphological evolution, though it is not yet known whether *upd-like* mediates its effects in *Nasonia* through JAK/STAT or other pathways. *Nasonia upd-like* appears to be particularly susceptible to wing growth–altering changes, which indicates that the gene might have a specialized role in specifying organ size in the growth gene network. Considering that many size and shape differences between animals are due to differences in cell numbers (*9*), *upd-like* genes could be hotspots of size and shape evolution in other species as well.

Using a phenotype-based positional cloning approach, we have identified two different major QTL genes (*wdw* and *ws1*) that are responsible for sex-specific differences in wing development between closely related *Nasonia* species. From what

is known about fly wing development (*22–24*), the alternative candidate gene approach would not have predicted the role of either *upd* or *dsx* in *Nasonia* wing size. Nevertheless, both genes appear to be homologs of functionally conserved developmental regulatory genes, which is consistent with the hypothesis that core developmental genes tend to be involved in morphological evolution (*25, 26*). It has also been argued that noncoding *cis*-regulatory changes could play a central role in developmental differences between species (*27, 28*). Our findings support this view and further implicate growth-regulating genes in organ-specific size and shape evolution.

References and Notes
1. G. Galilei, *Dialogues Concerning Two New Sciences*, H. Crew, A. De Salvio, Transls. (MacMillan, New York, 1914).
2. C. Darwin, *On the Origin of Species by Means of Natural Selection, or the Preservation of Favored Races in the Struggle for Life* (John Murray, London, 1859).
3. J. B. Losos, T. R. Jackman, A. Larson, K. Queiroz, L. Rodriguez-Schettino, *Science* **279**, 2115 (1998).
4. A. Abzhanov, M. Protas, B. R. Grant, P. R. Grant, C. J. Tabin, *Science* **305**, 1462 (2004).
5. S. W. McKechnie *et al.*, *Mol. Ecol.* **19**, 775 (2010).
6. M. D. Shapiro *et al.*, *Nature* **428**, 717 (2004).
7. D. L. Stern, V. Orgogozo, *Evolution* **62**, 2155 (2008).
8. D. W. Loehlin *et al.*, *PLoS Genet.* **6**, e1000821 (2010).
9. B. A. Edgar, *Nat. Rev. Genet.* **7**, 907 (2006).
10. T. Lecuit, L. Le Goff, *Nature* **450**, 189 (2007).
11. D. W. Loehlin, L. S. Enders, J. H. Werren, *Heredity* **104**, 260 (2010).
12. R. Raychoudhury *et al.*, *Heredity* **104**, 278 (2010).
13. J. H. Werren, D. W. Loehlin, in *Emerging Model Organisms*, vol. 2, D. A. Crotty, A. Gann, Eds. (Cold Spring Harbor Laboratory Press, Cold Spring Harbor, NY, 2009), pp. 267–298.
14. R. F. Weston, I. Qureshi, J. H. Werren, *J. Evol. Biol.* **12**, 586 (1999).
15. C. S. Raymond, M. W. Murphy, M. G. O'Sullivan, V. J. Bardwell, D. Zarkower, *Genes Dev.* **14**, 2587 (2000).
16. L. E. Sanders, M. N. Arbeitman, *Dev. Biol.* **320**, 378 (2008).
17. Materials and methods are available as supporting material on *Science* Online.
18. Supporting text is available as supporting material on *Science* Online.
19. J. S. Rawlings, K. M. Rosler, D. A. Harrison, *J. Cell Sci.* **117**, 1281 (2004).
20. J. H. Werren *et al.*, *Science* **327**, 343 (2010).
21. N. I. Arbouzova, M. P. Zeidler, *Development* **133**, 2605 (2006).
22. J. C. Hombría, S. Brown, S. Häder, M. P. Zeidler, *Dev. Biol.* **288**, 420 (2005).
23. T. Mukherjee, J. C. Hombría, M. P. Zeidler, *Oncogene* **24**, 2503 (2005).
24. C. C. Robinett, A. G. Vaughan, J. M. Knapp, B. S. Baker, *PLoS Biol.* **8**, e1000365 (2010).
25. T. Werner, S. Koshikawa, T. M. Williams, S. B. Carroll, *Nature* **464**, 1143 (2010).
26. B. R. Wasik, D. J. Rose, A. P. Moczek, *Evol. Dev.* **12**, 353 (2010).
27. D. L. Stern, *Evolution* **54**, 1079 (2000).
28. S. B. Carroll, *PLoS Biol.* **3**, e245 (2005).
29. R. Raychoudhury, L. Baldo, D. C. Oliveira, J. H. Werren, *Evolution* **63**, 165 (2009).

REPORTS

Field-Effect Tunneling Transistor Based on Vertical Graphene Heterostructures

L. Britnell,[1] R. V. Gorbachev,[2] R. Jalil,[2] B. D. Belle,[2] F. Schedin,[2] A. Mishchenko,[1] T. Georgiou,[1] M. I. Katsnelson,[3] L. Eaves,[4] S. V. Morozov,[5] N. M. R. Peres,[6,7] J. Leist,[8] A. K. Geim,[1,2]* K. S. Novoselov,[1]* L. A. Ponomarenko[1]*

An obstacle to the use of graphene as an alternative to silicon electronics has been the absence of an energy gap between its conduction and valence bands, which makes it difficult to achieve low power dissipation in the OFF state. We report a bipolar field-effect transistor that exploits the low density of states in graphene and its one-atomic-layer thickness. Our prototype devices are graphene heterostructures with atomically thin boron nitride or molybdenum disulfide acting as a vertical transport barrier. They exhibit room-temperature switching ratios of ≈50 and ≈10,000, respectively. Such devices have potential for high-frequency operation and large-scale integration.

The performance of graphene-based field effect transistors (FETs) has been hampered by graphene's metallic conductivity at the neutrality point (NP) and the unimpeded electron transport through potential barriers caused by Klein tunneling, which limit the achie-

vable ON-OFF switching ratios to ~10^3 and those achieved so far at room temperature to <10 (*1–7*). These low ratios are sufficient for individual high-frequency transistors and analog electronics (*4–7*), but they present a fundamental problem for any realistic prospect of graphene-based integrated circuits (*1–7*). A possible solution is to open a band gap in graphene—for example, by using bilayer

[1]School of Physics and Astronomy, University of Manchester, Manchester M13 9PL, UK. [2]Manchester Centre for Mesoscience and Nanotechnology, University of Manchester, Manchester M13 9PL, UK. [3]Institute for Molecules and Materials, Radboud University of Nijmegen, 6525 AJ Nijmegen, Netherlands. [4]School of Physics and Astronomy, University of Nottingham, Nottingham NG7 2RD, UK. [5]Institute for Microelectronics Technology, 142432 Chernogolovka, Russia. [6]Departamento de Física, Universidade do Minho, P-4710-057, Braga, Portugal. [7]Graphene Research Centre and Department of Physics, National University of Singapore, 2 Science Drive 3, 117542 Singapore. [8]Momentive Performance Materials, 22557 West Lunn Road, Strongsville, OH 44070, USA.

*To whom correspondence should be addressed. E-mail: geim@manchester.ac.uk (A.K.G.); kostya@manchester.ac.uk (K.S.N.); leonid.ponomarenko@manchester.ac.uk (L.A.P.)

graphene (8, 9), nanoribbons (10, 11), quantum dots (11), or chemical derivatives (12)—but it has proven difficult to achieve high ON-OFF ratios without degrading graphene's electronic quality.

We report an alternative graphene transistor architecture—namely, a field-effect transistor based on quantum tunneling (13–17) from a graphene electrode through a thin insulating barrier [in our case, hexagonal boron nitride (hBN) or molybdenum disulfide of ~1 nm thickness]. The operation of the device relies on the voltage tunability of the tunneling density of states (DOS) in graphene and of the effective height Δ of the tunnel barrier adjacent to the graphene electrode. To illustrate the proposed concept, we concentrate on graphene-hBN-graphene devices [an alternative barrier material (MoS$_2$) is discussed in (18)].

The structure and operational principle of our FET are shown in Fig. 1. For convenience of characterization, both source and drain electrodes were made from graphene layers in the multiterminal Hall bar geometry (18). This device configuration allowed us to not only measure the tunnel current-voltage curves (I-V) but also characterize the response of the graphene electrodes, thus providing additional information about the transistor operation. The core graphene-hBN-graphene structure was encapsulated in hBN so as to allow higher quality of the graphene electrodes (19, 20). To fabricate the device shown in Fig. 1A, we first used the standard cleavage technique (21) to prepare relatively thick hBN crystals on top of an oxidized Si wafer (300 nm of SiO$_2$), which acted as a gate electrode (Fig. 1 and fig. S1). The crystals served as a high-quality atomically flat substrate and a bottom encapsulation layer (19). Monolayer graphene (Gr$_B$) was then transferred onto a selected hBN crystal (20 to 50 nm thick) using a dry transfer procedure (19, 22). After deposition of metal contacts (5 nm Ti/50 nm Au) and etching to form a multiterminal Hall bar mesa, the structure was annealed at 350°C in forming gas. A few-atom-thick hBN crystal was identified (23) and transferred on top of Gr$_B$ by using the same procedures. This hBN layer served as the tunnel barrier. The whole process of positioning, annealing, and defining a Hall bar was repeated to make the second (top) graphene electrode (Gr$_T$). Last, a thick hBN crystal encapsulated the entire multilayer structure (Fig. 1A and fig. S1). Further details of our multistep fabrication procedures can be found in (18, 22). We tested devices with tunnel barriers having thickness d from 1 to 30 hBN layers (18). To illustrate the basic principle of the tunneling FETs, we focus on the data obtained from four devices with a tunnel barrier made of 4 to 7 layers and discuss the changes observed for other d.

When a gate voltage V_g was applied between the Si substrate and the bottom graphene layer (Gr$_B$), the carrier concentrations n_B and n_T in both bottom and top electrodes increased because of the weak screening by monolayer graphene (24), as shown schematically in Fig. 1C. The increase of the Fermi energy E_F in the graphene

layers could lead to a reduction in Δ for electrons tunneling predominantly at this energy (18). In addition, the effective height also decreased relative to the NP because the electric field penetrating through Gr$_B$ altered the shape of the barrier (25, 26). Furthermore, the increase in the tunneling DoS as E_F moved away from the NP (24) led to an increase in the tunnel current I. Depending on parameters, any of the above three contributions could dominate changes in I with varying V_g. We emphasize that the use of graphene in this device architecture is critical

Fig. 1. Graphene field-effect tunneling transistor. (**A**) Schematic structure of our experimental devices. In the most basic version of the FET, only one graphene electrode (Gr$_B$) is essential, and the outside electrode can be made from a metal. (**B**) The corresponding band structure with no gate voltage applied. (**C**) The same band structure for a finite gate voltage V_g and zero bias V_b. (**D**) Both V_g and V_b are finite. The cones illustrate graphene's Dirac-like spectrum and, for simplicity, we consider the tunnel barrier for electrons.

because this exploits graphene's low DOS, which for a given change in V_g led to a much greater increase in E_F as compared with a conventional two-dimensional gas with parabolic dispersion (13–17). This difference translated into much greater changes of both Δ and tunneling DOS.

The behavior of in-plane resistivity ρ for the Gr$_B$ and Gr$_T$ layers as a function of V_g is shown in Fig. 2A. The curves indicate little residual doping for encapsulated graphene (≈ 0 and $<10^{11}$ cm^{-2} for Gr$_B$ and Gr$_T$, respectively). In both layers, ρ strongly depended on V_g, showing that Gr$_B$ did not screen out the electric field induced by the Si-gate electrode. The screening efficiency was quantified by Hall effect measurements (Fig. 2, B to D), which showed that the gate induced approximately the same amount of charge in both layers at low concentrations—that is, there was little screening if n_B was small. As the concentration in Gr$_B$ increased, the $n_B(V_g)$ and $n_T(V_g)$ dependences became super- and sublinear, respectively (Fig. 2, B and C), because of the increase in n_B, which led to an increasingly greater
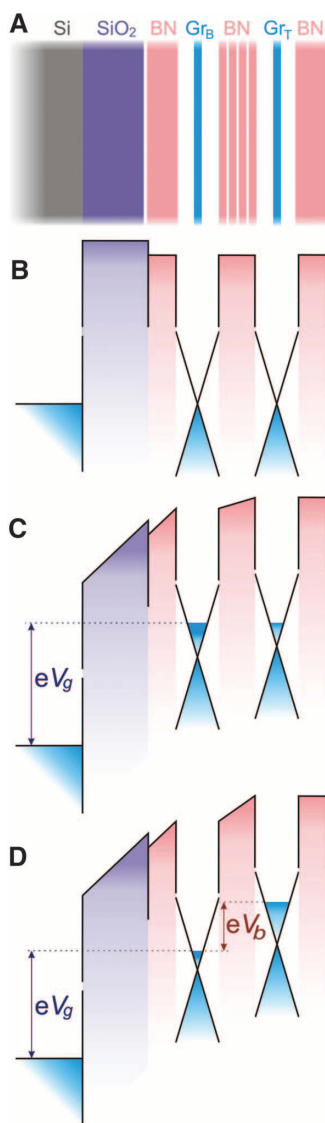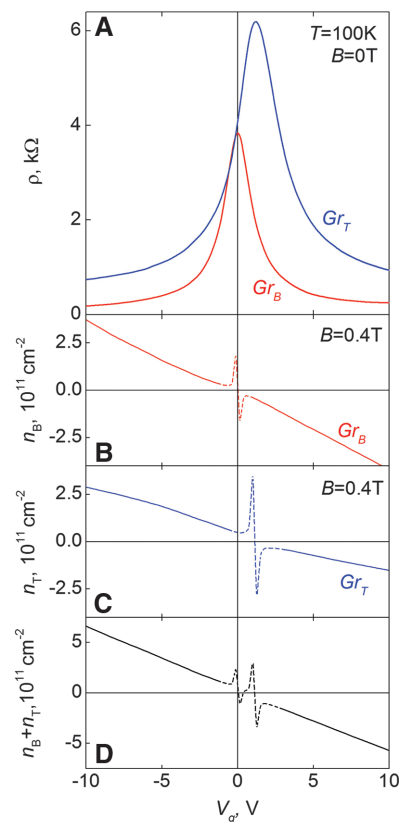

Fig. 2. Graphene as a tunneling electrode. (**A**) Resistivities of the source and drain graphene layers as a function of V_g. (**B** to **D**) Carrier concentrations in the two layers induced by gate voltage, which were calculated from the measured Hall resistivities ρ_{xy} by using the standard expression $n = B/e\rho_{xy}$, where B is the magnetic field and e is the electron charge. Close to the NP, the spikes appear (shown by dotted curves) because the above expression is not valid in the inhomogeneous regime of electron-hole puddles. The shown device has a 4-layer hBN barrier.

fraction of the gate-induced electric field being screened out by Gr_B (18). Hence, more electrons accumulated in the bottom graphene electrode, and fewer reached the top electrode. The total charge accumulated in both layers varied linearly in V_g (Fig. 2D), as expected. We could describe the observed redistribution of the charge between the two graphene layers in terms of the corresponding sequential circuit including the quantum capacitance (13, 27) of the graphene layers (fig. S2). For a parabolic band, the ratio between n_B and n_t would be independent on V_g, and therefore, the electric field penetrating into the tunnel barrier would be substantially reduced even in the limit of zero n_B (13).

A bias voltage V_b applied between Gr_B and Gr_T gave rise to a tunnel current through the thin hBN barrier that scaled with device area. I-V characteristics for one of our devices at various V_g are shown in Fig. 3A. First, we consider the case of zero V_g. At low V_b, I was linear in bias, yielding a tunnel resistivity $\rho^T = V_b/I \approx 100$ gigohms μm^2 for this hBN thickness. At higher voltages (V_b above ~0.1 V), I grew more rapidly. The I-V curves could be described (Fig. 3A, inset, and fig. S3) by the standard quantum-tunneling formulae (25, 26), assuming energy conservation but no momentum conservation at the mismatched graphene-hBN interface (28).

As shown below, we could distinguish experimentally between electron and hole tunneling and found that the tunneling was due to holes. This result is in agreement with a recent theory for the graphene-hBN interface (29), which reports a separation between the Dirac point in graphene and the top of the hBN valance band of ≈1.5 eV, whereas the conduction band is >4 eV away from the Dirac point. The fit to our data with Δ = 1.5 eV yielded a tunneling mass $m \approx 0.5\ m_0$ (m_0 is the free electron mass), which is in agreement with the effective mass for holes in hBN (30). Furthermore, our analysis indicated that I varied mainly with the change in the tunneling DOS, whereas the change in tunneling probability with applied bias was a secondary (albeit important) effect (18). For our atomically thin hBN barriers with relatively low ρ^T, we were not in a regime of exponential sensitivity to changes in $\Delta[E_F(V_b)]$.

We demonstrate transistor operation in Fig. 3A, which plots the influence of gate voltage on I. V_g substantially enhanced the tunnel current, and the changes were strongest at low bias. The field effect was rather gradual for all gate voltages up to ±50 V, a limit set by the electrical breakdown of our SiO_2 gate dielectric (typically ≈60 V). This response is quantified in Fig. 3B, which plots the low-bias tunneling conductivity $\sigma^T = I/V_b$ as a function of V_g. The influence of V_g was highly asymmetric: σ^T changed by a factor of ≈20 for negative V_g (holes) and by a factor of 6 for positive V_g (electrons). We observed changes up to ≈50 for hole tunneling in other devices and always the same asymmetry (fig. S4) (18). Also, the ON-OFF ratios showed little change between room and liquid-helium temperatures, as expected for Δ >> thermal energy.

To analyze the observed behavior of $\sigma^T(V_g)$, we modeled the zero-bias conductivity by using the relation $\sigma^T \propto DOS_B(V_g) \times DOS_T(V_g) \times T(V_g)$, where the indices refer to the two graphene layers and $T(V_g)$ is the transmission coefficient through the hBN barrier (25, 26). The resulting curve shown in Fig. 3B accounts qualitatively for the main features in the measured data, using
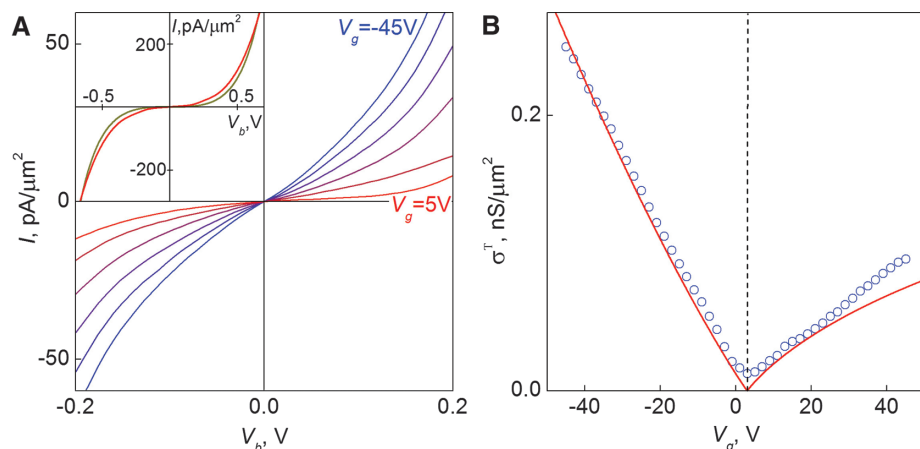
self-consistently the same tunneling parameters m and Δ given above. At V_g near zero, corresponding to tunneling from states near the NP, the tunneling DOS in both graphene layers was small and nonzero and was the result of residual doping, disorder, and temperature effects (18). The application of a gate voltage of either polarity led to a higher DOS and, therefore, higher σ^T. The gradual increase in $\sigma^T(V_g)$ for both polarities in Fig. 3B was therefore caused by the increasing DOS. However, V_g also affected the transmission coefficient. Because of the shift of E_F with changing V_g, the effective barrier height Δ decreased for one sign of charge carriers and increased for the other (Fig. 1B), which explains the asymmetry in both experimental and calculated $\sigma^T(V_g)$ in Fig. 3B in terms of the change in $T(V_g)$. For our devices, the effect of V_g on $T(V_g)$ was relatively weak (nonexponential) and comparable with the effect caused by changes in the tunneling DOS. The sign of the asymmetry infers that the hBN barrier height was lower for holes than for electrons, which is in agreement with the graphene-hBN band structure calculations (29). The weaker dependence of I on V_g at high bias can also be understood in terms of the more gradual increase in the tunneling DOS and in E_F at high doping ($V_b = 0.5V$ correspond to $n_B \approx 10^{13}\ cm^{-2}$).

Our results and analysis suggest that higher ON-OFF ratios could be achieved by using either higher V_g or making devices with larger d, so that the tunneling depends exponentially on bias and is controlled by the barrier height rather than the DOS. The former route is limited by the electrical breakdown of dielectrics at ~1 V/nm ($V_g \approx 300V$ for our SiO_2 thickness). By extrapolating the analysis shown in Fig. 3B to such voltages, we found that ON-OFF ratios >10^4 would be possible for our 4-to-7-layer devices if SiO_2 of highest quality were used. However, it would still require unrealistically large V_g to enter the regime where E_F becomes comparable with Δ and changes in $\sigma^T(V_g)$ are exponentially fast. Therefore, we explored the alternative option and investigated devices with both thinner and thicker hBN barriers. For 1- to 3-hBN layers, zero-bias σ^T increased exponentially with decreasing number of layers, which is consistent with quantum tunneling, and we observed a weaker influence of V_g on I, as expected for the more conductive regime. On the other hand, the thicker hBN barriers were prone to electrical breakdown. Nonetheless, for a few devices with d ≈ 6 to 9 nm, we were able to measure a tunnel current without breakdown. A current >10 pA appeared at biases of several volts and increased exponentially with V_b. The thicker devices' I-V characteristics could be fitted by using the same hole-tunneling parameters used above, thus indicating quantum tunneling rather than an onset of electrical breakdown. Unfortunately, no substantial changes (exceeding 50%) in the tunnel current could be induced by V_g. This insensitivity to gate voltage remains to be understood but was

Fig. 3. Tunneling characteristics for a graphene-hBN device with 6 ± 1 layers of hBN as the tunnel barrier. (**A**) I-Vs for different V_g (in 10-V steps). Because of finite doping, the minimum tunneling conductivity is achieved at $V_g \approx 3V$. The inset compares the experimental I-V at V_g = 5 V (red curve) with theory (dark), which takes into account the linear DOS in the two graphene layers and assumes no momentum conservation. Further examples of experimental curves and their fitting can be found in (18). (**B**) Zero-bias conductivity as a function of V_g. The symbols are experimental data, and the solid curve is our modeling. The curve is slightly shifted with respect to zero V_g because of remnant chemical doping. In all the calculations, we assumed the hole tunneling with m = 0.5 m_0 and Δ ≈ 1.5 eV (29, 30) and used d as measured by atomic force microscopy. Both I and σ are normalized per tunnel area, which was typically 10 to 100 μm^2 for the studied devices. Temperature, 240 K.

probably caused by charge traps that screened the influence of the gate.

An alternative method to achieve an exponential dependence of the tunneling current on gate voltage would be to use a barrier dielectric with a smaller Δ, which would be comparable with typical E_F realizable in graphene. One of such candidate materials is MoS_2, which has a band gap of about 1.3 eV and can be obtained in a mono- or few-layers state similar to hBN and graphene (*21*). Our first graphene-MoS_2–based devices demonstrate ON-OFF ratio close to 10.000 (fig. S5), which is sufficient for certain types of logic circuits.

We conclude that our tunneling devices offer a viable route for high-speed graphene-based analog electronics. The ON-OFF ratios already exceed those demonstrated for planar graphene FETs at room temperature by a factor of 10 (*3–7*). The transit time for the tunneling electrons through the nanometer-thick barriers is expected to be extremely fast (a few femtoseconds) (*13–17*) and exceeds the electron transit time in submicrometer planar FETs. It should also be possible to decrease the lateral size of the tunneling FETs down to the 10 nm scale, a requirement for integrated circuits. Furthermore, there appears to be no fundamental limitation

to further enhancement of the ON-OFF ratios by optimizing the architecture and by using higher-quality gate dielectrics and, in particular, lower tunnel barriers (Δ < maximum achievable E_F).

References and Notes

1. P. Avouris, Z. H. Chen, V. Perebeinos, *Nat. Nanotechnol.* **2**, 605 (2007).
2. A. K. Geim, *Science* **324**, 1530 (2009).
3. F. Schweirz, *Nat. Nanotechnol.* **5**, 487 (2010).
4. Y. Wu *et al.*, *Nature* **472**, 74 (2011).
5. L. Liao *et al.*, *Nature* **467**, 305 (2010).
6. S. J. Han *et al.*, *Nano Lett.* **11**, 3690 (2011).
7. Y. M. Lin *et al.*, *Science* **332**, 1294 (2011).
8. E. V. Castro *et al.*, *Phys. Rev. Lett.* **99**, 216802 (2007).
9. J. B. Oostinga, H. B. Heersche, X. Liu, A. F. Morpurgo, L. M. K. Vandersypen, *Nat. Mater.* **7**, 151 (2008).
10. M. Y. Han, B. Ozyilmaz, Y. B. Zhang, P. Kim, *Phys. Rev. Lett.* **98**, 206805 (2007).
11. C. Stampfer *et al.*, *Front. Phys.* **6**, 271 (2011).
12. D. C. Elias *et al.*, *Science* **323**, 610 (2009).
13. S. Luryi, *Appl. Phys. Lett.* **52**, 501 (1988).
14. M. Heiblum, M. V. Fischetti, *IBM J. Res. Develop.* **34**, 530 (1990).
15. J. A. Simmons *et al.*, *J. Appl. Phys.* **84**, 5626 (1998).
16. A. Zaslavsky *et al.*, *Appl. Phys. Lett.* **83**, 1653 (2003).
17. A. Sciambi *et al.*, *Phys. Rev. B* **84**, 085301 (2011).
18. Materials and methods are available as supporting material on *Science* Online.
19. C. R. Dean *et al.*, *Nat. Nanotechnol.* **5**, 722 (2010).
20. A. S. Mayorov *et al.*, *Nano Lett.* **11**, 2396 (2011).
21. K. S. Novoselov *et al.*, *Proc. Natl. Acad. Sci. U.S.A.* **102**, 10451 (2005).
22. L. A. Ponomarenko *et al.*, *Nat. Phys.* **7**, 958 (2011).
23. R. V. Gorbachev *et al.*, *Small* **7**, 465 (2011).
24. A. H. Castro Neto, F. Guinea, N. M. R. Peres, K. S. Novoselov, A. K. Geim, *Rev. Mod. Phys.* **81**, 109 (2009).
25. J. G. Simmons, *J. Appl. Phys.* **34**, 1793 (1963).
26. E. L. Wolf, *Principles of Electron Tunneling Spectroscopy* (Oxford Univ. Press, Oxford, 1985).
27. L. A. Ponomarenko *et al.*, *Phys. Rev. Lett.* **105**, 136801 (2010).
28. J. M. Xue *et al.*, *Nat. Mater.* **10**, 282 (2011).
29. N. Kharche, S. K. Nayak, *Nano Lett.* **11**, 5274 (2011).
30. Y. N. Xu, W. Y. Ching, *Phys. Rev. B* **44**, 7787 (1991).

The Local Structure of Amorphous Silicon

M. M. J. Treacy[1]* and K. B. Borisenko[2,3]

It is widely believed that the continuous random network (CRN) model represents the structural topology of amorphous silicon. The key evidence is that the model can reproduce well experimental reduced density functions (RDFs) obtained by diffraction. By using a combination of electron diffraction and fluctuation electron microscopy (FEM) variance data as experimental constraints in a structural relaxation procedure, we show that the CRN is not unique in matching the experimental RDF. We find that inhomogeneous paracrystalline structures containing local cubic ordering at the 10 to 20 angstrom length scale are also fully consistent with the RDF data. Crucially, they also matched the FEM variance data, unlike the CRN model. The paracrystalline model has implications for understanding phase transformation processes in various materials that extend beyond amorphous silicon.

Amorphous silicon (a-Si) can be regarded as a classic example of a disordered four-coordinated covalent material. Understanding its structure has implications for understanding structures and structure-properties correlations not only for similar covalently bonded networks but also for a wider range of other amorphous materials. In general, having the correct structural model of an amorphous state is important in order to understand the structural origins of glass transitions and associated phenomena. Previous studies rely on spatially heterogeneous dynamics

using either crystalline (*1*, *2*) or noncrystalline (*3*, *4*) inhomogeneities to explain kinetics of glass transitions and phenomena of glass-forming ability. Such knowledge is essential for a number of industrially important materials, such as phase-change memory materials for information storage (*5*, *6*). Accurate structural models are crucial for understanding mechanisms of deformation in metallic glasses (*7*). This knowledge is needed to ultimately build novel materials with the required properties. It is widely believed that the structure of a-Si is well represented by the continuous random network (CRN) model, which was first introduced by Zachariasen as a model for network glasses (*8*). The ideal CRN for a-Si is a fully four-coordinated, nonperiodic structure that is metastable with respect to crystalline silicon and is constructed primarily from five-, six- and seven-membered rings. Crystalline Si comprises six-

membered rings only. High-quality CRN models, which reproduce the experimental density, have been developed by applying bond-swapping algorithms (*9*, *10*), in conjunction with framework relaxation using appropriate potentials (*11*, *12*). The models generate a reduced density function (RDF) that matches the essential features of experimental data obtained by high-energy x-ray and neutron diffraction (*13*), as well as electron diffraction (*14*). In addition, the models broadly reproduce features observed in Raman spectra (*15*), as well as the vibrational density of states obtained by neutron diffraction (*12*, *16*).

Other models for a-Si have been proposed. The paracrystallite model of Hosemann and Baggchi (1962) (*17*) and the microcrystallite model of Turnbull and Polk (1972) (*18*) are generally discredited because they are thought to be inconsistent with RDF data. Both models describe materials containing small grains of ordered material that are just a few nanometers in extent, but in the paracrystallite model there are strain gradients throughout the grains. The width of the second peak in the RDF suggests a range of Si-Si-Si angles that is thought to be inconsistent with either type of crystalline order. However, it has been argued that fluctuation electron microscopy (FEM) data provide irrefutable evidence for the presence of substantial topological crystallinity in a-Si at the 10 to 20 Å length scale (*19*). Although the FEM evidence has been reproduced by several groups for various samples of a-Si that were amorphized by different methods (*20–22*), the presence of topologically crystalline ordering in a-Si is not widely accepted as it appears to contradict carefully conducted RDF experiments (*13*). It has been asserted that claims

[1]Department of Physics, Arizona State University, Tempe, AZ 85287, USA. [2]Department of Materials, University of Oxford, Parks Road, Oxford OX1 3PH, UK. [3]Research Complex at Harwell, Rutherford Appleton Laboratory, Harwell Oxford, Didcot OX11 0FA, UK.

*To whom correspondence should be addressed. E-mail: treacy@asu.edu

Science

Field-Effect Tunneling Transistor Based on Vertical Graphene Heterostructures

L. Britnell, R. V. Gorbachev, R. Jalil, B. D. Belle, F. Schedin, A. Mishchenko, T. Georgiou, M. I. Katsnelson, L. Eaves, S. V. Morozov, N. M. R. Peres, J. Leist, A. K. Geim, K. S. Novoselov and L. A. Ponomarenko

Tunnel Barriers for Graphene Transistors

Transistor operation for integrated circuits not only requires that the gate material has high-charge carrier mobility, but that there is also an effective way of creating a barrier to current flow so that the device can be switched off and not waste power. Graphene offers high carrier mobility, but the shape of its conduction and valence bands enables electron tunneling and makes it difficult to achieve low currents in an ''off'' state. **Britnell *et al.*** (p. 947, published online 2 February) have fabricated field-effect transistors in which a thin tunneling barrier created from a layered material—either hexagonal boron nitride or molybdenum disulfide—is sandwiched between graphene sheets. These devices exhibit on-off switching ratios of ≈50 and ≈10,000, respectively, at room temperature.

ARTICLE TOOLS	http://science.sciencemag.org/content/335/6071/947
SUPPLEMENTARY MATERIALS	http://science.sciencemag.org/content/suppl/2012/02/02/science.1218461.DC1
REFERENCES	This article cites 31 articles, 4 of which you can access for free http://science.sciencemag.org/content/335/6071/947#BIBL
PERMISSIONS	http://www.sciencemag.org/help/reprints-and-permissions

Use of this article is subject to the Terms of Service